doi:10.82124/CEAS-GNC-2026-074 CEAS-GNC-2026-074

Regularization and Control of the Circular Restricted Three-Body Problem using Birkhoff Coordinates: Applications to Orbital Transfers

Israe Zakaria[1] MASc Candidate, University of Toronto, Faculty of Applied Science & Engineering, Institute for Aerospace Studies (UTIAS), M3H 5T6, Toronto, Canada. israe.zakaria@mail.utoronto.ca

Christopher J. Damaren Professor and Director, University of Toronto, Faculty of Applied Science & Engineering, Institute for Aerospace Studies (UTIAS), M3H 5T6, Toronto, Canada. chris.damaren@utoronto.ca

ABSTRACT

This paper presents a formulation of the Circular Restricted Three-Body Problem (CR3BP) in Birkhoff coordinates, with applications to trajectory design and optimal control near the Earth-Moon system. The dynamical equations are explicitly derived in the Birkhoff framework and validated through numerical comparison with the classical rotating frame formulation. The stability characteristics of periodic orbits around all five Lagrange points are analyzed, highlighting the improved linearization behavior of the Birkhoff formulation near the collinear equilibria. Differential correction techniques are used to compute Lyapunov orbits, which serve as reference trajectories for transfer design. Several optimal control problems are solved, including transfers between Lyapunov orbits near L_1 and L_2, between distinct periodic orbits near L_5, and within the L_1 family. Performance comparisons in both coordinate systems reveal that the Birkhoff formulation offers superior numerical stability and supports larger transfer domains near unstable points under equivalent linearizations. These findings demonstrate the formulation's potential for robust cislunar trajectory design and its relevance to future mission planning.

Keywords: CR3BP; Birkhoff regularization; Lyapunov orbits; optimal control; cislunar transfers

Nomenclature

Classical CR3BP Variables

m_1, m_2	=	Masses of the two primary bodies
μ	=	Mass ratio parameter ($\mu = m_2/(m_1 + m_2)$)
x, y	=	Non-dimensional rotating-frame coordinates
$\dot{x}, \dot{y}$	=	Velocities in rotating frame (d/dt)
r_1, r_2	=	Distances from the particle to the primary bodies

[1]**Corresponding author:** Israe Zakaria, israe.zakaria@mail.utoronto.ca

t	=	Non-dimensional time in rotating frame
Ω	=	Effective potential in rotating frame
C	=	Jacobi constant
A	=	Linearized dynamics matrix (Jacobian of the system)
λ_i	=	Eigenvalues of A (local stability indicators)
L_1–L_5	=	Lagrange equilibrium points

Birkhoff Regularized Variables

u, v	=	Birkhoff-regularized coordinates
u', v'	=	Velocities in Birkhoff frame ($d/d\tau$)
τ	=	Pseudo-time in Birkhoff formulation
ρ_1, ρ_2, ρ_3	=	Regularized distance terms
N	=	Regularization factor in Birkhoff formulation
Ω^*	=	Regularized potential function

1 Introduction

The Circular Restricted Three-Body Problem (CR3BP) describes the motion of a particle of infinitesimal mass under the gravitational influence of two primary bodies in circular orbit about their barycenter. As a foundational model in astrodynamics, it underpins the design of cislunar trajectories, libration-point missions, and station-keeping strategies, with renewed relevance to current cislunar operations such as NASA's Gateway and Artemis programs.

In the classical formulation, the CR3BP is expressed in a rotating reference frame where the primaries remain fixed along the x-axis. This system admits five equilibrium solutions; known as the Lagrange points; around which families of periodic orbits exist. These orbits are widely used in mission design, such as the halo orbit of the *James Webb Space Telescope* around the Earth–Sun L_2 point. However, the dynamics near the collinear points (L_1, L_2, L_3) are strongly nonlinear and sensitive to initial conditions, and singularities occur at the primaries, degrading numerical accuracy near their vicinity.

Several transformations have been proposed to regularize these singularities. The Levi-Civita transformation [1] provides a quadratic regularization of the planar restricted two-body problem by mapping the singularity to a regular point through a conformal coordinate change and a time reparametrization known as the Sundman transformation [2]. Its spatial extension, the Kustaanheimo–Stiefel (KS) transformation [3, 4], lifts the three-dimensional Cartesian space into a four-dimensional space while performing a similar time regularization. Both the Levi-Civita and KS approaches are *local* regularizations: they remove only one singularity at a time, and are therefore not global in the sense of Szebehely [5]. In the CR3BP, Birkhoff introduced a conformal transformation that maps the singularities at *both* primaries to infinity while preserving the Hamiltonian structure of the system [5–7]. Other global regularization approaches for the restricted three-body problem include the coordinate systems proposed by Thiele [8] and Lemaître [9], as well as the unified conformal-mapping framework developed by Deprit and Broucke [10] and further refined by Broucke [11], who showed that apparently distinct regularization schemes can be expressed in a common mathematical form. A comprehensive treatment of these techniques is found in Szebehely's classical text [5] and the more recent review by Deprit *et al.* [12].

Despite these theoretical developments, the application of regularization to trajectory design and optimal control in multi-body dynamics has remained limited until recently. In the two-body setting, KS regularization has been applied to N-impulse transfer design [13, 14], low-thrust trajectory optimization via Pontryagin's minimum principle [15, 16], convex optimization-based maneuver planning [17], the gravity-perturbed Lambert problem [18], Lyapunov-based orbit control [19, 20], analytical orbit propa-

gation [21], uncertainty quantification [22], and accurate orbit propagation for planetary protection [23]. In the three-body problem, KS transformations have been used for dynamical systems analysis of nearly rectilinear halo orbits [24] and for the detection of close encounters in the elliptic restricted three-body problem using fast Lyapunov indicators [25]. LeGrand *et al.* [26] applied KS-regularized dynamics to Bayesian angles-only tracking in cislunar space, demonstrating the advantage of singularity-free equations for uncertainty propagation near the Moon.

The growing interest in cislunar operations has motivated significant advances in multi-body trajectory optimization. Russell [27] applied primer vector theory to global low-thrust trade studies, while Lantoine [28] developed a robust optimization methodology for low-thrust trajectories in multi-body environments. Direct collocation techniques for low-thrust transfers were systematically treated by Pritchett [29]. Sidhoum and Oguri [30] introduced an indirect forward–backward shooting method for low-thrust optimization in complex dynamics and compared smoothing methods for indirect trajectory optimization [31]. Tour design in multi-body systems has been addressed by Campagnola *et al.* [32] for the Europa Clipper mission, and the dynamics of transfers between cislunar and Sun–Earth libration points were studied by Boudad [33] in a four-body model. Bosanac [34] investigated how natural dynamical structures can be leveraged for transfer design in multi-body systems. Most recently, Oguri [35] presented a unified framework that combines both local (KS) and global (Thiele, Birkhoff, Lemaître) regularization with Pontryagin's minimum principle to solve low-thrust trajectory optimization problems in cislunar space, demonstrating that regularization-based formulations can find complex transfers involving close flybys of both primaries without requiring good initial guesses.

This paper fills a complementary gap by reformulating the CR3BP in Birkhoff coordinates to achieve a regularized and numerically stable representation of the dynamics, with a focus on feedback control and linearization-based transfer design rather than open-loop optimal control. The transformation from the classical rotating frame to the Birkhoff-regularized framework is derived, along with analytical expressions for the derivatives required in the equations of motion. The formulation is validated by simulating periodic Lyapunov orbits in both frameworks and mapping the regularized trajectories back to the classical frame for comparison. The five equilibrium (Lagrange) points are computed and their stability analyzed through eigenvalues. The practical utility of the approach is demonstrated through controlled trajectory design and orbit transfers around both unstable collinear points (L_1, L_2) and the stable triangular point (L_5). Results show that the Birkhoff formulation improves numerical stability and yields linearizations suitable for control over larger transfer domains, particularly near the unstable collinear regions.

2 Problem Formulation

2.1 Classical CR3BP Setup

The Circular Restricted Three-Body Problem (CR3BP) describes the motion of an infinitesimal particle m_3 under the gravitational attraction of two massive bodies m_1 and m_2, called the *primaries*, which revolve in circular orbits about their common barycenter. A comprehensive derivation of the CR3BP equations can be found in standard references such as Koon et al. [36].

In a dimensional inertial frame (X, Y), the distance between the primaries is D, and G denotes the gravitational constant. The system is nondimensionalized using the characteristic units of length D, mass $m_1 + m_2$, and time $\sqrt{D^3/G(m_1 + m_2)}$. This yields the dimensionless mass ratio

$$\mu = \frac{m_2}{m_1 + m_2}, \qquad m_1 = \mu, \quad m_2 = -1 + \mu. \tag{1}$$

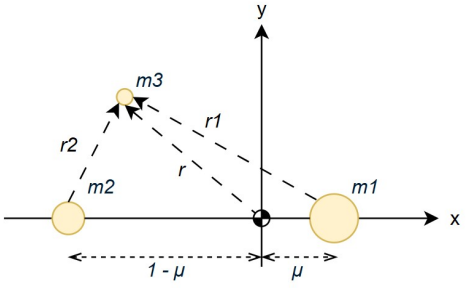

Fig. 1 Geometry of the CR3BP in the rotating frame.

In the rotating (synodic) frame (x, y), which co-rotates with the primaries at angular velocity $\omega = 1$, the more massive body m_1 is fixed at $x = -\mu$ and the less massive m_2 at $x = 1 - \mu$. In this frame, the third body experiences gravitational, Coriolis, and centrifugal forces, and its equations of motion are

$$\ddot{x} - 2\dot{y} = \frac{\partial \Omega}{\partial x}, \tag{2}$$

$$\ddot{y} + 2\dot{x} = \frac{\partial \Omega}{\partial y}, \tag{3}$$

where the effective potential is

$$\Omega(x, y) = \frac{1}{2}(x^2 + y^2) + \frac{1 - \mu}{r_1} + \frac{\mu}{r_2}, \tag{4}$$

and

$$r_1 = \sqrt{(x - \mu)^2 + y^2}, \qquad r_2 = \sqrt{(x + 1 - \mu)^2 + y^2}. \tag{5}$$

For numerical integration, the second-order equations are rewritten as a first-order system:

$$Y = \begin{bmatrix} x \\ y \\ v_x \\ v_y \end{bmatrix}, \qquad \dot{Y} = \begin{bmatrix} v_x \\ v_y \\ 2v_y + \dfrac{\partial \Omega}{\partial x} \\ -2v_x + \dfrac{\partial \Omega}{\partial y} \end{bmatrix},$$

with

$$\frac{\partial \Omega}{\partial x} = x - \frac{(1 - \mu)(x - \mu)}{r_1^3} - \frac{\mu(x + 1 - \mu)}{r_2^3}, \qquad \frac{\partial \Omega}{\partial y} = y - \frac{(1 - \mu)y}{r_1^3} - \frac{\mu y}{r_2^3}.$$

For uncontrolled motion, the CR3BP admits a conserved energy-like integral known as the Jacobi constant,

$$C = 2\Omega(x, y) - (\dot{x}^2 + \dot{y}^2), \tag{6}$$

which defines the zero-velocity surfaces and bounds the regions of possible motion. This formulation is directly integrated in nondimentionalized time t using adaptive Runge–Kutta schemes (e.g., `ode45`).

2.2 Birkhoff Regularization of the CR3BP

Birkhoff introduced a conformal transformation [5, 6] to remove the singularities that appear in the classical Circular Restricted Three-Body Problem (CR3BP) at the positions of the primaries, where the effective potential $\Omega(x, y)$ diverges. The mapping transfers the singular points to infinity in an auxiliary complex plane while preserving the analytic and Hamiltonian structure of the system.

Let the complex coordinate in the rotating frame be $z = x + iy$, and define an auxiliary complex variable $w = u + iv$. Birkhoff proposed the transformation

$$z = f(w) = \frac{w^2 + \mu(1 - \mu)}{2w + 1 - 2\mu}, \tag{7}$$

which maps the primary masses at $z = \mu$ and $z = -1 + \mu$ to infinity in the w-plane, thus eliminating the singularities globally.

The explicit mapping from the Birkhoff coordinates (u, v, τ) to the classical frame (x, y, t) is given by

$$\begin{aligned} x &= \tfrac{1}{2}\Big(u - \tfrac{1}{2} + \mu\Big) + \tfrac{1}{8}\cdot\frac{u + \frac{1}{2} - \mu}{(u + \frac{1}{2} - \mu)^2 + v^2}, \\ y &= \tfrac{1}{2}v - \tfrac{1}{8}\cdot\frac{v}{(u + \frac{1}{2} - \mu)^2 + v^2}, \\ \frac{dt}{d\tau} &= \frac{\rho_1^2\rho_2^2}{4\rho_3^4}, \end{aligned} \tag{8}$$

where

$$\rho_1 = \sqrt{(u-\mu)^2 + v^2}, \quad \rho_2 = \sqrt{(u+1-\mu)^2 + v^2}, \quad \rho_3 = \sqrt{(u + \tfrac{1}{2} - \mu)^2 + v^2}.$$

The only singularity occurs at $\rho_3 = 0$, corresponding to $w = -\frac{1}{2} + \mu$, which maps to spatial infinity.

Regularized Equations of Motion.

In the Birkhoff frame, the CR3BP dynamics take the form

$$\frac{d^2u}{d\tau^2} - 2N\dot{v} = \frac{\partial\Omega^*}{\partial u}, \qquad \frac{d^2v}{d\tau^2} + 2N\dot{u} = \frac{\partial\Omega^*}{\partial v}, \tag{9}$$

where

$$N = \frac{\rho_1^2\rho_2^2}{4\rho_3^4}, \qquad \Omega^*(u,v) = N\left[\frac{(1-\mu)\rho_1^2 + \mu\rho_2^2}{8\rho_3^2} + 2\rho_3\left(\frac{\mu}{\rho_1^2} + \frac{1-\mu}{\rho_2^2}\right) - \frac{1}{2}C\right].$$

For uncontrolled trajectories, the Jacobi constant remains conserved and is expressed in Birkhoff coordinates as:

$$C = 2\Omega^*(u,v) - \frac{1}{N}\left[\left(\frac{du}{d\tau}\right)^2 + \left(\frac{dv}{d\tau}\right)^2\right],$$

For numerical integration using adaptive Runge–Kutta schemes, the second-order regularized equations are reformulated as a first-order system along the pseudo-time τ:

$$Y = \begin{bmatrix} u \\ v \\ \dot{u} \\ \dot{v} \end{bmatrix}, \qquad \dot{Y} = \begin{bmatrix} \dot{u} \\ \dot{v} \\ 2N\,\dot{v} + \dfrac{\partial\Omega^*}{\partial u} \\ -2N\,\dot{u} + \dfrac{\partial\Omega^*}{\partial v} \end{bmatrix},$$

Inverse and Velocity Transformation (Present Work).

While Birkhoff provided the forward transformation (8), its inverse was not explicitly formulated. In this work, the inverse mapping is derived by inverting the complex function $z = f(w)$ of Eq. (7). This yields a quadratic in w:

$$w^2 - 2zw + \mu(1-\mu) - z(1-2\mu) = 0,$$

whose two roots w_1 and w_2 represent conjugate pre-images of each classical point (x, y). Both map back to the same spatial position, confirming the conformal symmetry and non-bijective nature of the transformation. The two branches of the inverse mapping are therefore:

$$w_{1,2} = z \pm \sqrt{z^2 - \mu(1-\mu) + z(1-2\mu)}.$$

To obtain consistent velocity mappings, the Jacobian of the transformation is computed as:

$$J(u,v) = \begin{bmatrix} \partial x/\partial u & \partial x/\partial v \\ \partial y/\partial u & \partial y/\partial v \end{bmatrix}, \quad \begin{bmatrix} \dot{u} \\ \dot{v} \end{bmatrix} = J^{-1}(u,v) \begin{bmatrix} v_x \\ v_y \end{bmatrix} \frac{dt}{d\tau}.$$

This formulation enables complete state transformation between the classical and regularized frames.

Validation via Lyapunov Orbit Reconstruction.

A Lyapunov orbit around the libration point L_1 in the Earth–Moon system ($\mu = 0.01215$) was first simulated in the classical rotating frame. The corresponding initial conditions were then transformed into the Birkhoff plane, yielding the two conjugate inverse roots w_1 and w_2. Each set of initial conditions was independently propagated in the regularized frame along the pseudo-time τ. The resulting trajectories were mapped back to the classical coordinates, where both reconstructions coincided with the original Lyapunov orbit to machine precision (maximum error $< 4\times10^{-16}$, $\sim 1.7\,\epsilon_{\text{mach}}$), confirming the numerical consistency and reversibility of the Birkhoff transformation (Fig. 2).

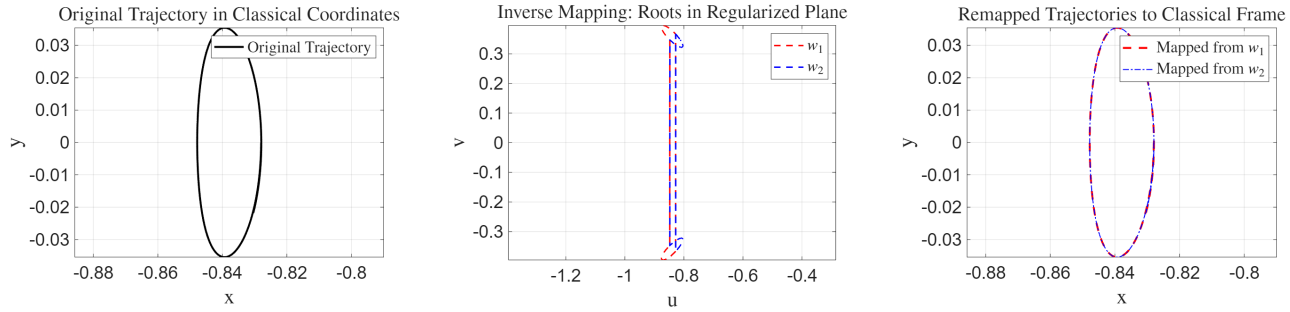

Fig. 2 Validation of the inverse Birkhoff transformation. The inverse mapping yields two branches in the Birkhoff plane, both of which reconstruct the same spatial trajectory.

The complete analytical developments underlying this section ; including the derivation of the regularized equations of motion from Birkhoff's conformal mapping, the formulation of the regularized potential $\Omega^*(u,v)$, the corresponding partial derivatives, Jacobians, and time reparameterization are provided in Appendices A-C.

3 Linear Stability Analysis of Equilibrium Points

3.1 Equilibrium Points in the Classical Frame

The Circular Restricted Three-Body Problem (CR3BP) admits five equilibrium solutions, known as the Lagrange points L_1–L_5, defined by $\dot{x} = \dot{y} = 0$ and $\ddot{x} = \ddot{y} = 0$. Substituting into the equations of motion (2) and (3) yields:

$$\frac{\partial \Omega}{\partial x} = x - \frac{(1-\mu)(x-\mu)}{r_1^3} - \frac{\mu(x+1-\mu)}{r_2^3} = 0, \qquad \frac{\partial \Omega}{\partial y} = y\left(1 - \frac{1-\mu}{r_1^3} - \frac{\mu}{r_2^3}\right) = 0.$$

From the y-equilibrium condition, setting $y = 0$ yields the three collinear points L_1, L_2, L_3, while imposing $r_1 = r_2$ defines the triangular points L_4 and L_5. For the Earth–Moon system ($\mu = 0.01213$), the corresponding equilibrium coordinates are:

$$L_1 = (-0.837, 0), \quad L_2 = (-1.156, 0),$$

$$L_3 = (1.005, 0), \quad L_{4,5} = (-0.488, \mp 0.866),$$

as illustrated in Fig. 3.

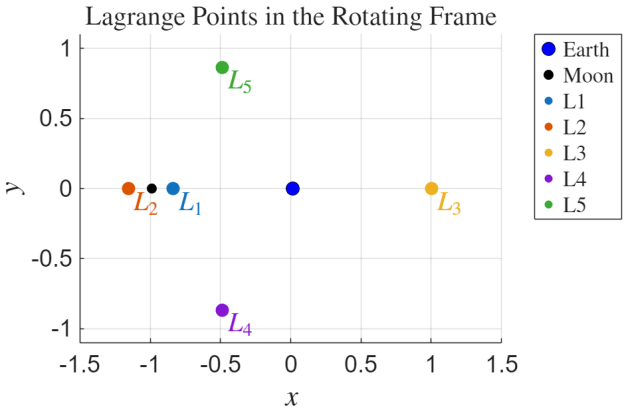

Fig. 3 Equilibrium points in the rotating frame.

3.2 Equilibrium Points in the Regularized Birkhoff Frame

In the Birkhoff-regularized formulation, equilibrium points correspond to stationary solutions of the regularized equations of motion, where $\dot{u} = \dot{v} = 0$ and $\ddot{u} = \ddot{v} = 0$. Substituting these conditions into the regularized dynamics (9) gives

$$\frac{\partial \Omega^*}{\partial u} = 0, \qquad \frac{\partial \Omega^*}{\partial v} = 0,$$

.

We solve this nonlinear system using a Newton–Raphson scheme for the gradient $\nabla\Omega^*(u, v)$, and the resulting equilibria are mapped back to the classical frame through the explicit Birkhoff transformation (8). The procedure yields five equilibrium points in the Birkhoff plane, identical to those of the classical CR3BP when transformed back to (x, y), confirming the analytical equivalence of both formulations.

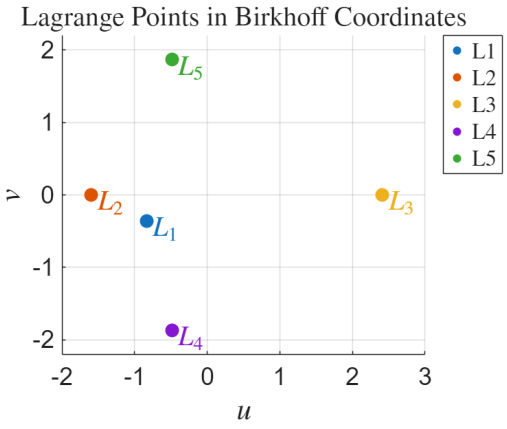

Fig. 4 Equilibrium points in the Birkhoff plane.

Table 2 Lagrange points obtained from the Birkhoff formulation.

Point	(u, v)	(x, y)	$\|\nabla\Omega^*\|$
L_1	(−0.837,−0.358)	(−0.837,0.000)	4.1×10^{-16}
L_2	(−1.598,0.000)	(−1.156,0.000)	1.4×10^{-16}
L_3	(2.412,0.000)	(1.005,0.000)	5.2×10^{-17}
L_4	(−0.488,−1.866)	(−0.488,−0.866)	2.2×10^{-16}
L_5	(−0.488,1.866)	(−0.488,0.866)	2.2×10^{-16}

3.3 Linear Stability in Classical and Regularized Frames

To assess local dynamics near each equilibrium, the system is linearized as $\dot{\mathbf{z}} = A\mathbf{z}$, with state vector $\mathbf{z} = [x,\ y,\ \dot{x},\ \dot{y}]^\top$ (or $[u,\ v,\ \dot{u},\ \dot{v}]^\top$). The Jacobian matrices are

$$A_{\text{classical}} = \begin{bmatrix} 0 & 0 & 1 & 0 \\ 0 & 0 & 0 & 1 \\ \Omega_{xx} & \Omega_{xy} & 0 & 2 \\ \Omega_{yx} & \Omega_{yy} & -2 & 0 \end{bmatrix}, \qquad A_{\text{Birkhoff}} = \begin{bmatrix} 0 & 0 & 1 & 0 \\ 0 & 0 & 0 & 1 \\ \Omega^*_{uu} & \Omega^*_{uv} & 0 & -N(u,v) \\ \Omega^*_{vu} & \Omega^*_{vv} & N(u,v) & 0 \end{bmatrix}. \tag{10}$$

The eigenvalues of A define local behavior: real parts correspond to exponential growth or decay (instability), while imaginary parts indicate oscillatory motion. The spectra computed in both frames are shown below:

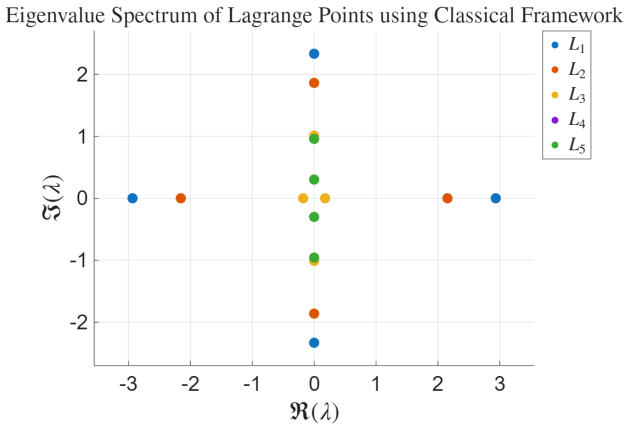

Fig. 5 Eigenvalue spectrum in the classical frame.

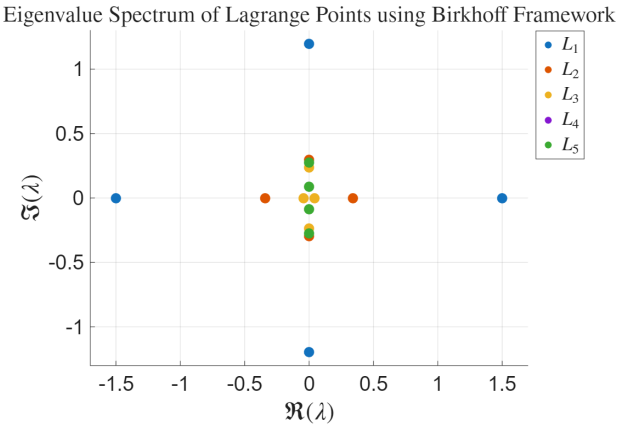

Fig. 6 Eigenvalue spectrum in the Birkhoff frame.

Both analyses yield identical stability behavior: L_1, L_2, L_3 exhibit saddle–center instability with one real and one imaginary eigenvalue pair, while L_4, L_5 possess two purely imaginary pairs and remaining linearly stable for $\mu < \mu_{\text{crit}} \approx 0.0385$, as satisfied by the Earth–Moon system. The identical eigenvalue spectra confirm that Birkhoff regularization preserves the intrinsic stability characteristics of the CR3BP, validating its consistency for subsequent control and transfer-orbit design.

4 Numerical Validation and Energy Conservation

The Birkhoff formulation was validated through uncontrolled orbit simulations in the Earth–Moon and Sun–Jupiter CR3BP systems. All integrations were performed using the regularized equations of motion in (u, v, τ), with trajectories mapped back to the classical rotating frame (x, y, t) for comparison. The Jacobi constant C was evaluated in both formulations to assess numerical accuracy and energy preservation.

4.1 Planar Lyapunov Orbits around the Collinear Equilibrium Points

A planar Lyapunov orbit near L_1 was computed using a single-shooting differential-correction method following Koon *et al.* [36]. Starting from $Y_0 = [x_0, 0, 0, v_{y0}]^\top$, the residual $r = x(t_f) - x_0$ was reduced iteratively as

$$v_{y0}^{(k+1)} = v_{y0}^{(k)} - \frac{r}{\partial x(t_f)/\partial v_{y0}},$$

until $|r| < 10^{-10}$. The corrected initial state, $Y_{0,L_1} = [-0.828,\ 0,\ 0,\ -0.08107]$, was integrated in both formulations and the mapped trajectories compared.

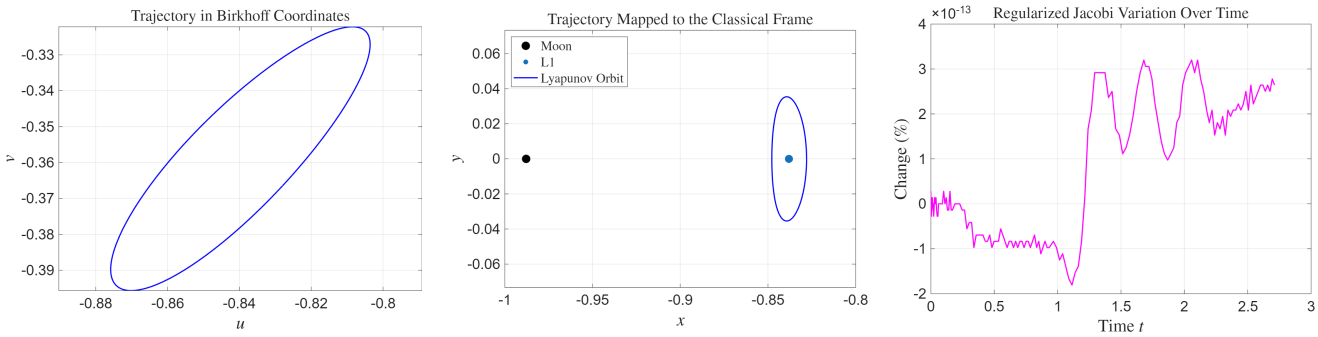

Fig. 7 Lyapunov orbit around L_1: simulated in Birkhoff coordinates and mapped to classical frame.

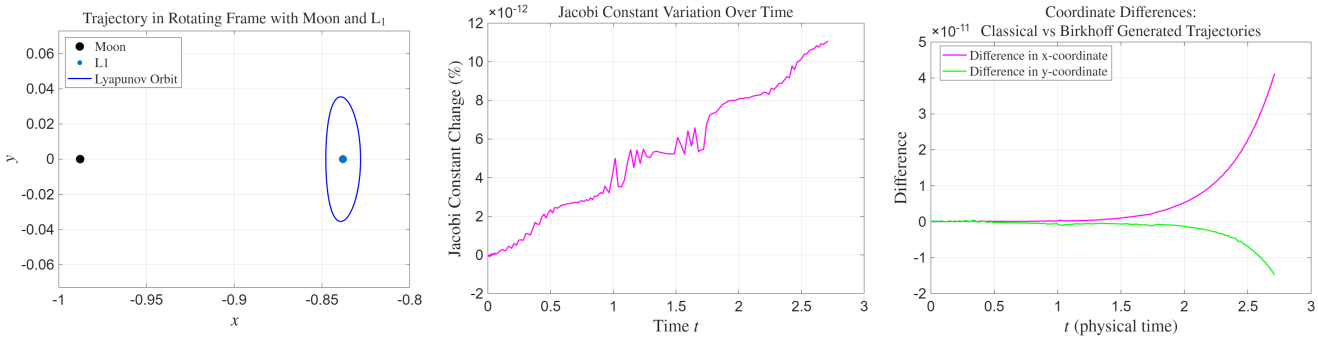

Fig. 8 Lyapunov orbit around L_1: simulated in classical coordinates, compared to the mapped trajectory.

The mapped trajectory matches the classical CR3BP orbit within 10^{-11} after one period, with the error growing exponentially due to local instability. The Jacobi constant variation is about one order of magnitude smaller in Birkhoff coordinates, while in the classical formulation the error grows linearly. Similar results were obtained for the orbits around L_2 and L_3, indicating an improved numerical conditioning and energy stability near the unstable collinear points.

Beyond energy conservation, we evaluate the conditioning of the linearized system along a 100-orbit L_1 Lyapunov family. The Jacobian $A(t)$ is computed along each trajectory, and its condition number is defined as $\mathrm{cond}(A) = \sigma_{\max}(A)/\sigma_{\min}(A)$. Figure 9 shows $\mathrm{cond}(A)$ over one normalized period. The Birkhoff representation consistently exhibits lower mean condition numbers and reduced dispersion, with an average improvement of approximately a factor of 2–3. This indicates a less anisotropic and more numerically robust linearization, providing a quantitative explanation for the improved stability observed in the Birkhoff formulation.

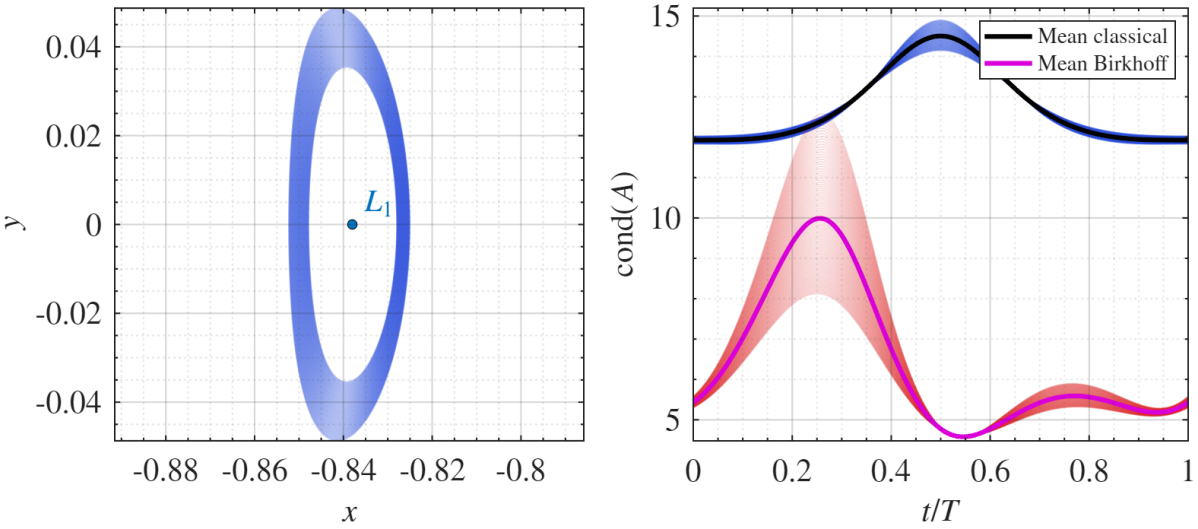

Fig. 9 Condition number of the linearized dynamics along the L_1 Lyapunov family.

4.2 Periodic and Quasi-periodic Orbits around the Triangular Equilibrium Points

The Birkhoff formulation was further validated at the triangular Lagrange points L_4 and L_5, which correspond to stable equilibria in both the Earth–Moon and Sun–Jupiter CR3BP systems. Two representative cases were analyzed: a small periodic orbit in the Earth–Moon system and a large-amplitude quasi-periodic Trojan orbit in the Sun–Jupiter system.

a) The periodic orbit around L_5, initialized at $Y_{0,2} = [-0.5257, 0.8392, -0.0061, -0.00042]$, was obtained from the action–angle normal form and simulated in both frameworks.

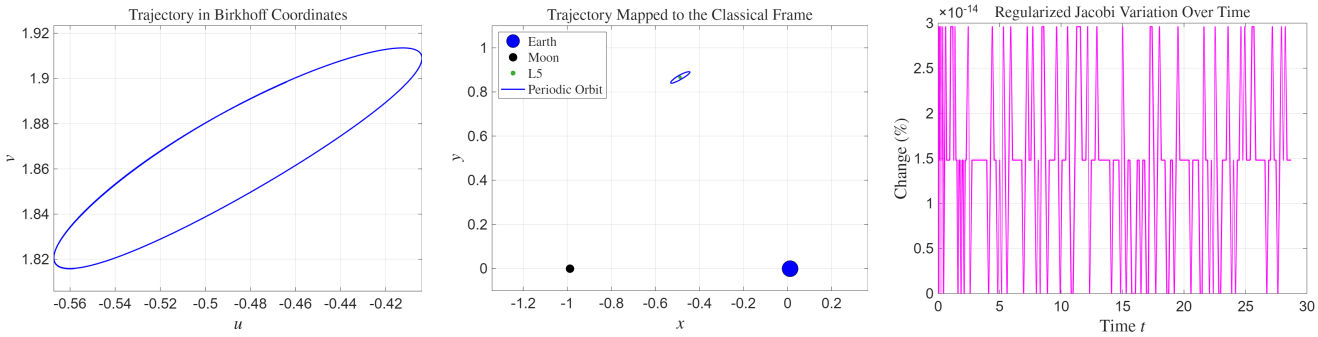

Fig. 10 Periodic orbit around L_5: simulated in Birkhoff coordinates, mapped to the classical frame, and validated via Jacobi conservation.

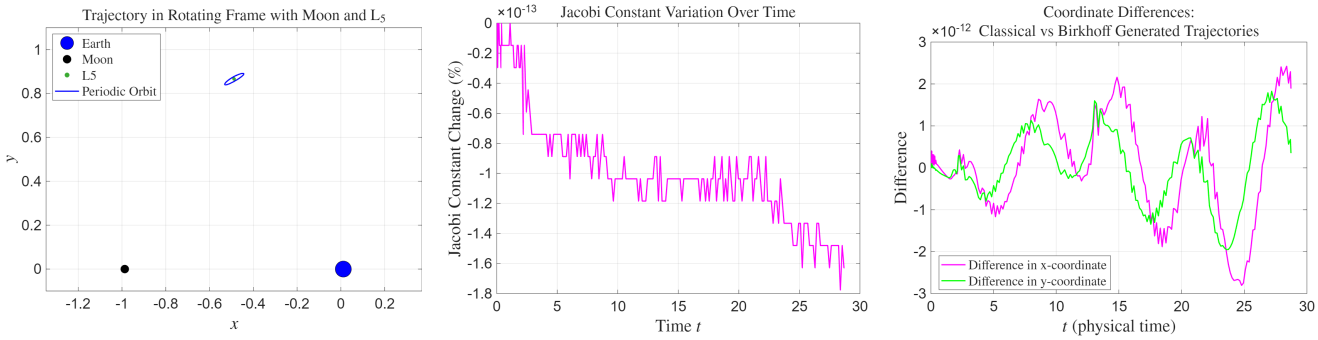

Fig. 11 Classical simulation and comparison with the mapped Birkhoff trajectory.

The Jacobi constant exhibited a variation one order of magnitude smaller in the regularized formulation (10^{-14} vs. 10^{-13}). In the Birkhoff integration, the variation remained bounded with a smooth oscillatory pattern, while in the classical formulation it grew monotonically. The coordinate difference stayed below 10^{-12} and displayed a bounded quasi-oscillatory behavior with a dominant frequency, possibly associated with the intrinsic stability of the L_5 region.

b) A large-amplitude tadpole (Trojan) orbit was simulated in the Sun–Jupiter CR3BP ($\mu = 9.539 \times 10^{-4}$) using $Y_0 = [-0.625, 0.9, 0, 0]$.

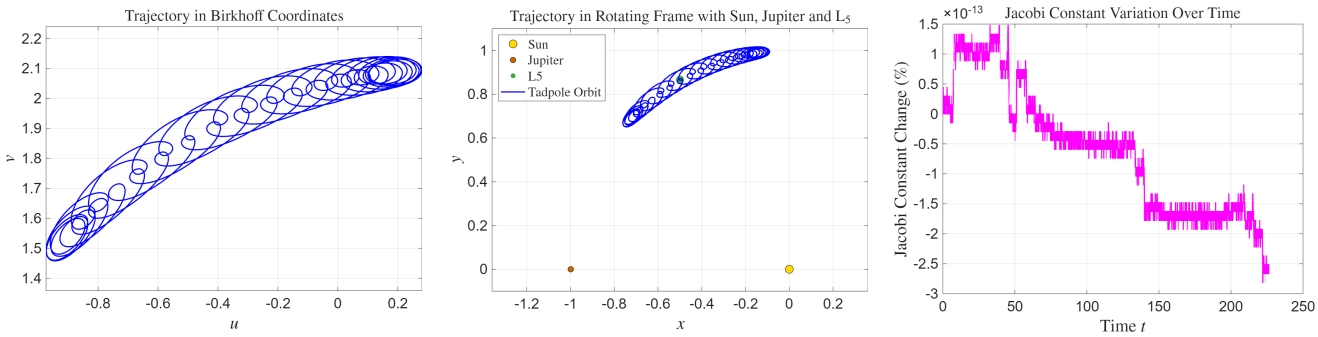

Fig. 12 Birkhoff simulation of tadpole-like Trojan orbit around L_5.

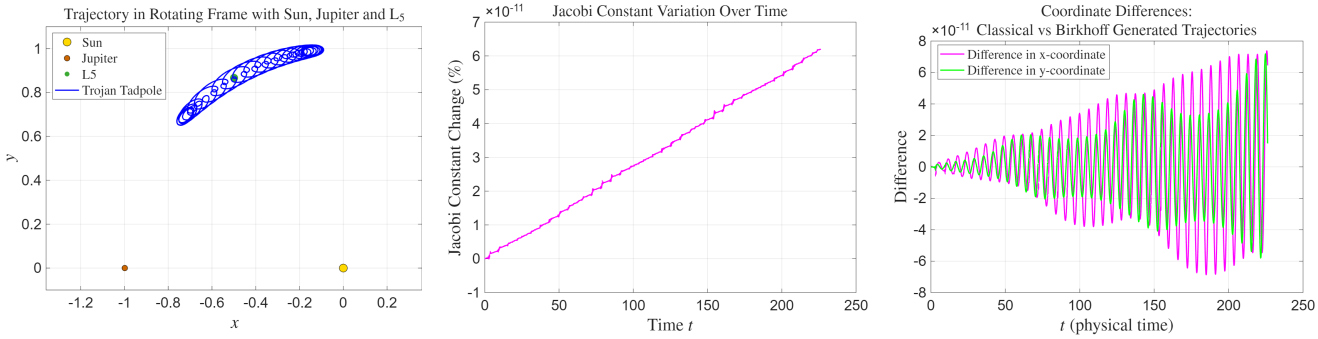

Fig. 13 Classical integration and comparison with Birkhoff results for the Trojan orbit.

Both formulations produced nearly identical trajectories over long integration times. The Jacobi constant variation was two orders of magnitude smaller in the regularized formulation (10^{-13} vs. 10^{-11}), with the Birkhoff case exhibiting a bounded quasi-oscillatory behavior, while the classical drift increased linearly. The coordinate difference remained below 10^{-11} and showed a slow growth modulated by a two-frequency quasi-oscillatory pattern, characteristic of Trojan motion around L_5.

5 Optimal Control of Orbital Transfers in Classical and Regularized CR3BP Frameworks

Beyond improving numerical stability, the Birkhoff regularization also enables a more robust formulation for control applications in the CR3BP. This section investigates the use of the Linear Quadratic Regulator (LQR) for orbital transfer design, comparing control performance in both frameworks.

5.1 Linear Quadratic Regulator (LQR) Strategy

The Linear Quadratic Regulator (LQR) provides an optimal feedback law that minimizes control effort while guiding the system along a desired trajectory. Here, a time-varying LQR (TV-LQR) is implemented in both the classical and regularized formulations to evaluate how each linearization influences control performance.

Linearizing the nonlinear CR3BP dynamics about a reference trajectory yields

$$\dot{Y} = A(t)Y + B\,u,$$

where $A(t)$ is the time-dependent Jacobian (Eq. 10). The input matrix $B \in \mathbb{R}^{4\times2}$ couples the control accelerations to the state derivatives and is defined as

$$B = \begin{bmatrix} 0 & 0 \\ 0 & 0 \\ 1 & 0 \\ 0 & 1 \end{bmatrix}, \qquad u = \begin{bmatrix} u_x \\ u_y \end{bmatrix} \text{ in the classical frame, or } u = \begin{bmatrix} u_u \\ u_v \end{bmatrix} \text{ in the regularized frame.}$$

At each integration step, the linearized model is updated and the algebraic Riccati equation

$$A^\top P + PA - PBR^{-1}B^\top P + Q = 0$$

is solved for the current $A(t)$, yielding a frozen-time steady-state gain

$$K(t) = R^{-1}B^\top P(t).$$

The resulting feedback law

$$u(t) = -K(t)\,[Y(t) - Y_{\text{ref}}(t)]$$

continuously adapts to the local dynamics as the linearization evolves along the trajectory. The LQR formulation is chosen not as a candidate flight algorithm, but as a controlled benchmark: because the same controller structure and cost functional are applied in both coordinate systems, differences in convergence and transfer range isolate the effect of the underlying linearization rather than algorithmic sophistication.

5.2 Time-Varying LQR Transfer Between Periodic Orbits Near L_5

A controlled transfer between two periodic orbits near L_5 was used to evaluate the performance of the time-varying LQR controller. The initial conditions for the two reference orbits are

$$Y_{0,1} = \begin{bmatrix} -0.50310617 \\ 0.84556552 \\ -0.02240453 \\ -0.00016385 \end{bmatrix}, \qquad Y_{0,2} = \begin{bmatrix} -0.52567259 \\ 0.83921119 \\ -0.00610191 \\ -0.00042197 \end{bmatrix}.$$

In the classical frame, a time-variable gain ($Q = \text{diag}(1, 1, 1, 1)$, $R = 0.1I$) stabilized the trajectory between Orbit 1 and Orbit 2, producing convergence in position, velocity, and energy (Fig. 14).

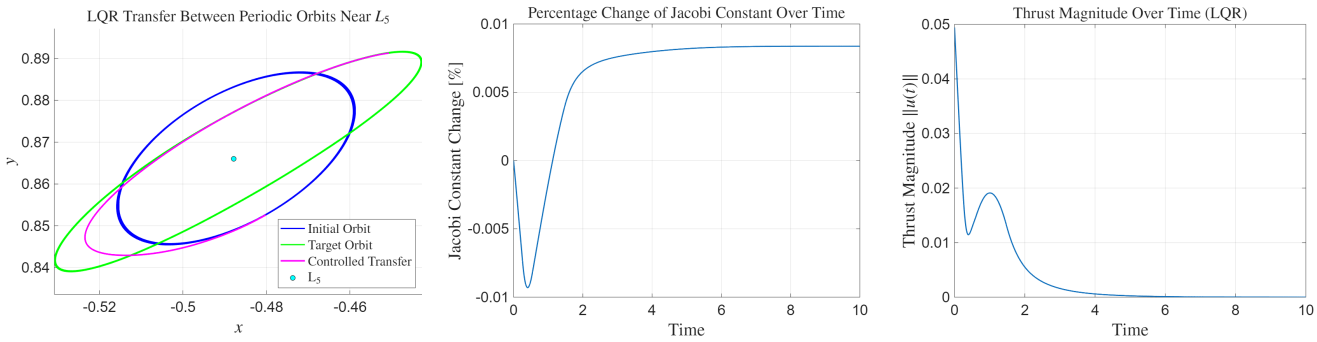

Fig. 14 TV-LQR based orbital transfer in the classical CR3BP.

The same transfer was repeated using the Birkhoff formulation with adaptive gain ($Q = \text{diag}(1, 1, 1, 1)$, $R = 100I$).

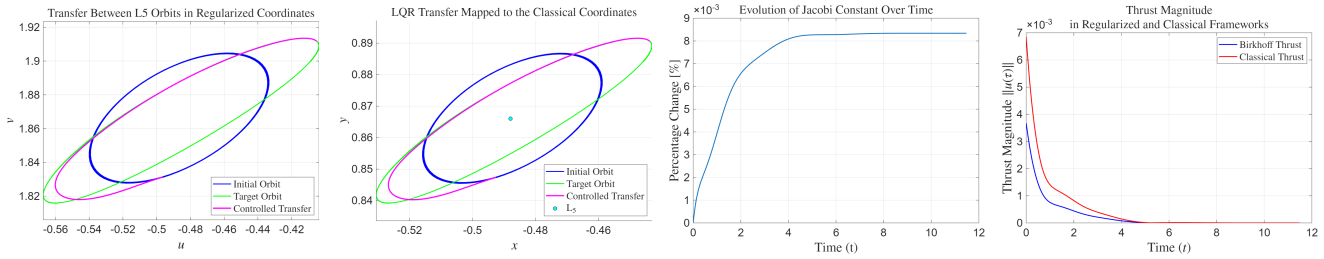

Fig. 15 TV-LQR based orbital transfer in the regularized CR3BP.

Both controllers achieved successful convergence to the target orbit, exhibiting comparable maximum thrust magnitudes when expressed on the same classical scale ($\|u_{\max}\|_{\text{Birkhoff, remapped}} \approx 5 \times 10^{-3}$, $\|u_{\max}\|_{\text{classical}} \approx 5 \times 10^{-2}$). However, the regularized formulation produced a smoother control profile, characterized by a continuously decaying thrust magnitude and monotonic Jacobi convergence. In contrast, the classical implementation exhibited two distinct thrust peaks, one at initiation and a secondary bump mid-transfer, corresponding to transient deviations in energy adjustment.

5.3 Time-Varying LQR Transfers within the L_1 Orbit Family

To assess the benefits of Birkhoff regularization for long-range control, two matched L_1 Lyapunov orbit families were generated by continuation and differential correction, comprising 5000 orbits with a step size of $\Delta x = 3 \times 10^{-5}$. Each classical orbit was analytically mapped to its regularized counterpart using the inverse Birkhoff transformation.

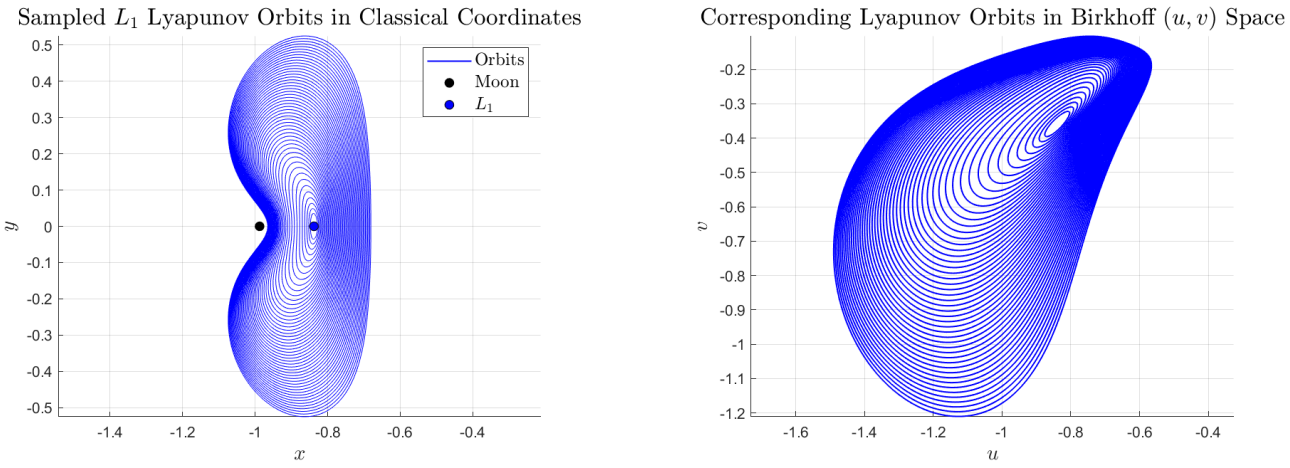

Fig. 16 Matched L_1 Lyapunov orbit families in the classical and Birkhoff formulations.

Controlled transfers were performed using the frozen-time TV-LQR in both formulations. In the classical frame ($Q = \text{diag}(10, 10, 1, 1)$, $R = 0.1I$, control saturated at $\|u\|_{\max} = 0.01$), convergence was achieved only between nearby orbits, with reachable transfers limited to approximately 46 orbits. In the Birkhoff formulation ($Q = \text{diag}(1000, 1000, 1, 1)$, $R = 100I$), stable transfers were achieved across the entire 5000-orbit family. No choice of weights in the classical frame produced convergence beyond approximately 46 orbits; beyond this threshold the trajectory diverges from the orbit family entirely.

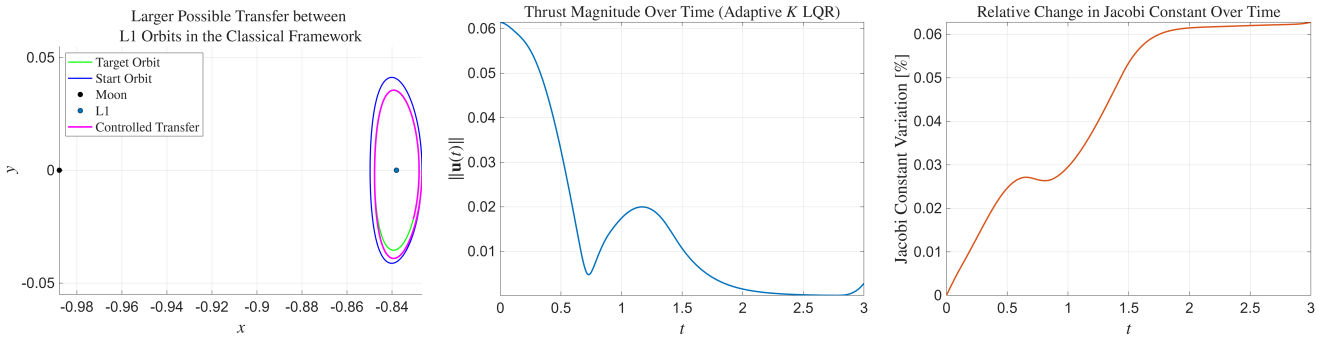

Fig. 17 Time-varying LQR controlled transfers in the classical CR3BP for the L_1 Lyapunov family. From left to right: transfer trajectory, thrust magnitude, and Jacobi constant variation.

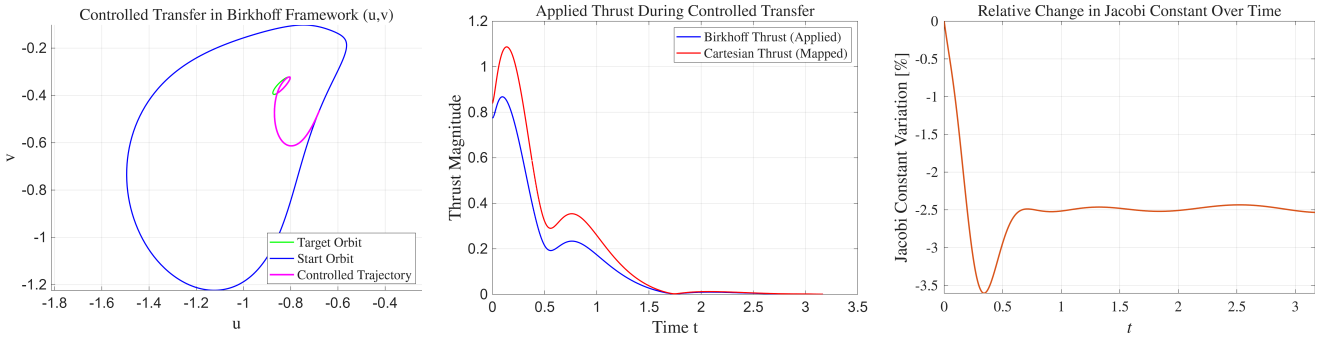

Fig. 18 Time-varying LQR controlled transfers in the Birkhoff-regularized CR3BP for the L_1 Lyapunov family. From left to right: transfer trajectory, thrust magnitude, and Jacobi constant variation.

This reflects the wider validity region of the regularized linearization, which remains well-conditioned near the collinear points where the classical Jacobian degrades due to proximity to the primary singularities.

6 Conclusion

This work presented the Birkhoff regularized formulation of the Circular Restricted Three-Body Problem (CR3BP) and demonstrated its advantages for guidance and control applications. The derived equations remove singularities at the primaries while preserving the Hamiltonian structure, yielding improved numerical conditioning and energy conservation.

Validation through Lyapunov and Trojan orbits confirmed dynamic equivalence with the classical model and reduced Jacobi drift by one to two orders of magnitude.

Time-varying LQR control laws were then applied to orbital transfers, showing that the Birkhoff linearization enables smoother thrust profiles and stable convergence across wider orbital domains than the classical formulation.

In practice, the classical formulation remains suitable for short-duration analyses away from the primaries, whereas the Birkhoff formulation is preferred for long-duration trajectories, close approaches, and control applications, where it prevents the accumulation of numerical errors in the Jacobians and improves robustness.

Ongoing work employs direct pseudospectral optimal control methods to globally optimize transfer trajectories in the regularized framework, and extends the dynamics to the Bicircular Restricted Four-Body Problem (BR4BP) for multi-body mission design. The planar formulation will subsequently be generalized to three-dimensional dynamics using the B3 transformation [37, 38], which extends the Birkhoff conformal mapping to spatial coordinates via quaternion algebra.

Appendix

Appendix A: Birkhoff's Conformal Transformation and Regularization of the Equations of Motion

This appendix presents the derivation of a conformal transformation that regularizes the equations of motion in the planar circular restricted three-body problem (CR3BP), following the approach first introduced by Birkhoff [6].

Generalized Equations of Motion

We begin with the generalized second-order form of the equations of motion in a rotating frame with Coriolis-like terms:

$$\begin{cases} \dfrac{d^2x}{dt^2} - 2\lambda(x,y)\dfrac{dy}{dt} = U_x(x,y), \\ \dfrac{d^2y}{dt^2} + 2\lambda(x,y)\dfrac{dx}{dt} = U_y(x,y), \end{cases} \tag{11}$$

where $U(x, y)$ is the effective potential, and $\lambda(x, y)$ encodes the rotational velocity field (in CR3BP, $\lambda = 1$). The total mechanical energy is: In the CR3BP, energy conservation is replaced by the Jacobi integral:

$$\left(\frac{dx}{dt}\right)^2 + \left(\frac{dy}{dt}\right)^2 = 2U(x,y). \tag{12}$$

We also define the arc length differential:

$$ds^2 = dx^2 + dy^2. \tag{13}$$

Conformal Mapping and Coordinate Change

To regularize the singularities of the system, we introduce a conformal coordinate transformation:

$$\zeta = x + iy = f(w), \quad \text{with } w = u + iv, \tag{14}$$

where $f(w)$ is an analytic function. This implies $f'(w)$ exists and the transformation is angle-preserving. The differential is:

$$d\zeta = f'(w)\, dw \Rightarrow dx + idy = f'(w)(du + idv). \tag{15}$$

Taking real and imaginary parts:

$$dx = \mathrm{Re}(f'(w))\, du - \mathrm{Im}(f'(w))\, dv, \tag{16}$$

$$dy = \mathrm{Im}(f'(w))\, du + \mathrm{Re}(f'(w))\, dv. \tag{17}$$

The arc length becomes:

$$ds^2 = dx^2 + dy^2 = |f'(w)|^2(du^2 + dv^2) \Rightarrow ds = |f'(w)|\, ds_1. \tag{18}$$

Time Transformation and Energy Preservation

To preserve the structure of the energy integral under the conformal map, we apply the chain rule:

$$\frac{dx}{dt} = \mathrm{Re}(f'(w))\frac{du}{d\tau} - \mathrm{Im}(f'(w))\frac{dv}{d\tau}, \tag{19}$$

$$\frac{dy}{dt} = \mathrm{Im}(f'(w))\frac{du}{d\tau} + \mathrm{Re}(f'(w))\frac{dv}{d\tau}. \tag{20}$$

Substituting into the energy relation:

$$\left(\frac{dx}{dt}\right)^2 + \left(\frac{dy}{dt}\right)^2 = |f'(w)|^2 \left(\left(\frac{du}{d\tau}\right)^2 + \left(\frac{dv}{d\tau}\right)^2\right). \tag{21}$$

To match the form of the Jacobi integral, we define the time transformation:

$$dt = |f'(w)|^2 \, d\tau, \tag{22}$$

which leads to the regularized energy form:

$$\left(\frac{du}{d\tau}\right)^2 + \left(\frac{dv}{d\tau}\right)^2 = 2\Omega(x, y)\,|f'(w)|^2. \tag{23}$$

Regularized Equations of Motion in (u, v) Coordinates

We now differentiate the velocities with respect to τ and transform the Coriolis terms accordingly:

$$\frac{d^2u}{d\tau^2} = \frac{d}{d\tau}\left(\frac{du}{d\tau}\right), \tag{24}$$

$$\frac{d^2v}{d\tau^2} = \frac{d}{d\tau}\left(\frac{dv}{d\tau}\right), \tag{25}$$

$$-2\lambda(x, y)\frac{dy}{dt} = -2\lambda(x, y)\,|f'(w)|^2\frac{dv}{d\tau}, \tag{26}$$

$$+2\lambda(x, y)\frac{dx}{dt} = +2\lambda(x, y)\,|f'(w)|^2\frac{du}{d\tau}. \tag{27}$$

We define the transformed potential:

$$\Omega^*(u, v) = \Omega(x(u, v), y(u, v))\,|f'(w)|^2, \tag{28}$$

and its gradient:

$$[\Omega^*]_u = \frac{\partial}{\partial u}\left(\Omega(x, y)\,|f'(w)|^2\right), \tag{29}$$

$$[\Omega^*]_v = \frac{\partial}{\partial v}\left(\Omega(x, y)\,|f'(w)|^2\right). \tag{30}$$

The resulting regularized equations of motion in (u, v, τ) are:

$$\begin{cases} \dfrac{d^2u}{d\tau^2} - 2\lambda(x,y)\,|f'(w)|^2\dfrac{dv}{d\tau} = \left[\Omega(x,y)\,|f'(w)|^2\right]_u, \\ \dfrac{d^2v}{d\tau^2} + 2\lambda(x,y)\,|f'(w)|^2\dfrac{du}{d\tau} = \left[\Omega(x,y)\,|f'(w)|^2\right]_v, \\ \left(\dfrac{du}{d\tau}\right)^2 + \left(\dfrac{dv}{d\tau}\right)^2 = 2\Omega(x,y)\,|f'(w)|^2. \end{cases} \tag{31}$$

This system is now regular at previously singular points, particularly at the primaries, and is suitable for both analytical study and numerical integration.

Choice of $f(w)$ in the CR3BP

Birkhoff's original construction chose the conformal mapping transformation:

$$f(w) = \frac{w^2 + \mu(1-\mu)}{2w + 1 - 2\mu}, \tag{32}$$

with its analytic derivative:

$$f'(w) = \frac{2(w-\mu)(w+1-\mu)}{(2w+1-2\mu)^2}. \tag{33}$$

This choice maps the primary singularities to finite, regular points in the (u, v)-plane. The factors $(w-\mu)$ and $(w+1-\mu)$ in the numerator cancel the poles in Ω_x and Ω_y, ensuring singularity-free behavior across the domain. This defines a complete framework for regularizing the CR3BP equations of motion.

Appendix B: Derivation and Validation of $\Omega^*(u, v)$ and Its Derivatives

This appendix provides a complete derivation of the regularized potential function $\Omega^*(u, v)$, along with its gradient and Hessian, used in the Birkhoff formulation of the Circular Restricted Three-Body Problem (CR3BP). We also present numerical validation via finite differences.

B.1 Definition of the Regularized Potential

In the Birkhoff formulation of the Circular Restricted Three-Body Problem (CR3BP), the regularized effective potential $\Omega^*(u, v)$ is defined as:

$$\Omega^*(u, v) = N(u, v) \left[\Omega(u, v) - \frac{1}{2} C \right],$$

where:

- $N(u, v) = \dfrac{\rho_1^2 \rho_2^2}{4\rho_3^4}$ is the regularized potential in Birkhoff formulation,
- $\Omega(u, v)$ is the rotating-frame effective potential composed of two terms:

$$\Omega(u, v) = \Omega_1 + \Omega_2,$$

$$\Omega_1 = \frac{(1-\mu)\rho_1^4 + \mu\rho_2^4}{8\rho_3^2},$$
$$\Omega_2 = 2\rho_3 \left(\frac{\mu}{\rho_2^2} + \frac{1-\mu}{\rho_1^2} \right).$$

- $C = 2\Omega(u_0, v_0) - \dfrac{1}{N(u_0, v_0)} \left(\dot{u}_0^2 + \dot{v}_0^2 \right)$ is the Jacobi constant at a reference state $(u_0, v_0, \dot{u}_0, \dot{v}_0)$.

We define the distances ρ_1, ρ_2, and ρ_3 in the Birkhoff plane as follows:

$$a_1 = u - \mu, \quad a_2 = u + 1 - \mu, \quad a_3 = u + \tfrac{1}{2} - \mu,$$

$$\rho_1 = \sqrt{a_1^2 + v^2}, \quad \rho_2 = \sqrt{a_2^2 + v^2}, \quad \rho_3 = \sqrt{a_3^2 + v^2}.$$

B.2 Gradient Derivation

We derive the gradient of the regularized potential $\Omega^*(u, v)$ using the product rule:

$$\frac{\partial \Omega^*}{\partial u} = \frac{\partial N}{\partial u}\left(\Omega - \tfrac{1}{2}C\right) + N \cdot \frac{\partial \Omega}{\partial u}, \quad \frac{\partial \Omega^*}{\partial v} = \frac{\partial N}{\partial v}\left(\Omega - \tfrac{1}{2}C\right) + N \cdot \frac{\partial \Omega}{\partial v}.$$

To compute this, we first evaluate the necessary intermediate derivatives.

Step 1: Regularization factor $N(u, v) = \frac{\rho_1^2 \rho_2^2}{4\rho_3^4}$

Using the product and quotient rules:

$$\frac{\partial N}{\partial u} = \frac{1}{4}\left[\frac{2a_1 \cdot \rho_2^2 + 2a_2 \cdot \rho_1^2}{\rho_3^4} - \frac{4a_3 \cdot \rho_1^2 \rho_2^2}{\rho_3^6}\right],$$
$$\frac{\partial N}{\partial v} = \frac{1}{4}\left[\frac{2v(\rho_1^2 + \rho_2^2)}{\rho_3^4} - \frac{4v \cdot \rho_1^2 \rho_2^2}{\rho_3^6}\right]$$

Step 2: Potential term $\Omega_1 = \frac{(1-\mu)\rho_1^4 + \mu\rho_2^4}{8\rho_3^2}$

Using the quotient and chain rules:

$$\frac{\partial \Omega_1}{\partial u} = \frac{(1-\mu) \cdot 4\rho_1^2 \cdot 2a_1 + \mu \cdot 4\rho_2^2 \cdot 2a_2}{8\rho_3^2} - \frac{[(1-\mu)\rho_1^4 + \mu\rho_2^4] \cdot 2a_3}{8\rho_3^4},$$
$$\frac{\partial \Omega_1}{\partial v} = \frac{(1-\mu) \cdot 4\rho_1^2 \cdot 2v + \mu \cdot 4\rho_2^2 \cdot 2v}{8\rho_3^2} - \frac{[(1-\mu)\rho_1^4 + \mu\rho_2^4] \cdot 2v}{8\rho_3^4}$$

Step 3: Potential term $\Omega_2 = 2\rho_3\left(\frac{\mu}{\rho_2^2} + \frac{1-\mu}{\rho_1^2}\right)$

Using the product and chain rules:

$$\frac{\partial \Omega_2}{\partial u} = 2\left[\frac{a_3}{\rho_3}\left(\frac{\mu}{\rho_2^2} + \frac{1-\mu}{\rho_1^2}\right) - \rho_3\left(\frac{2\mu a_2}{\rho_2^4} + \frac{2(1-\mu)a_1}{\rho_1^4}\right)\right],$$
$$\frac{\partial \Omega_2}{\partial v} = 2\left[\frac{v}{\rho_3}\left(\frac{\mu}{\rho_2^2} + \frac{1-\mu}{\rho_1^2}\right) - \rho_3\left(\frac{2\mu v}{\rho_2^4} + \frac{2(1-\mu)v}{\rho_1^4}\right)\right]$$

Step 4: Total gradient of $\Omega(u, v)$

$$\frac{\partial \Omega}{\partial u} = \frac{\partial \Omega_1}{\partial u} + \frac{\partial \Omega_2}{\partial u}, \quad \frac{\partial \Omega}{\partial v} = \frac{\partial \Omega_1}{\partial v} + \frac{\partial \Omega_2}{\partial v}$$

Step 5: Final expression for the gradient of $\Omega^*(u, v)$

Substituting all intermediate derivatives:

$$\boxed{\frac{\partial \Omega^*}{\partial u} = \frac{\partial N}{\partial u}\left(\Omega - \tfrac{1}{2}C\right) + N \cdot \frac{\partial \Omega}{\partial u}}$$

$$\boxed{\frac{\partial \Omega^*}{\partial v} = \frac{\partial N}{\partial v}\left(\Omega - \tfrac{1}{2}C\right) + N \cdot \frac{\partial \Omega}{\partial v}}$$

These expressions are essential for computing variational dynamics, stability analysis, and control in the Birkhoff-regularized CR3BP framework.

B.3 Hessian Derivation

We compute the second-order derivatives of the regularized potential $\Omega^*(u, v)$ using the product rule for multivariate functions:

$$\frac{\partial^2\Omega^*}{\partial u^2} = \frac{\partial^2 N}{\partial u^2}(\Omega - \tfrac{1}{2}C) + 2\frac{\partial N}{\partial u}\frac{\partial \Omega}{\partial u} + N\frac{\partial^2\Omega}{\partial u^2},$$

$$\frac{\partial^2\Omega^*}{\partial u\partial v} = \frac{\partial^2 N}{\partial u\partial v}(\Omega - \tfrac{1}{2}C) + \frac{\partial N}{\partial u}\frac{\partial \Omega}{\partial v} + \frac{\partial N}{\partial v}\frac{\partial \Omega}{\partial u} + N\frac{\partial^2\Omega}{\partial u\partial v},$$

$$\frac{\partial^2\Omega^*}{\partial v^2} = \frac{\partial^2 N}{\partial v^2}(\Omega - \tfrac{1}{2}C) + 2\frac{\partial N}{\partial v}\frac{\partial \Omega}{\partial v} + N\frac{\partial^2\Omega}{\partial v^2}.$$

Step 1: Second-order derivatives of the regularization factor $N(u, v) = \frac{\rho_1^2\rho_2^2}{4\rho_3^4}$

$$\frac{\partial^2 N}{\partial u^2} = \frac{1}{4}\left[\frac{2\rho_2^2 + 4a_1^2\rho_2^2 + 2\rho_1^2 + 4a_2^2\rho_1^2}{\rho_3^4} - \frac{8a_3(2a_1\rho_2^2 + 2a_2\rho_1^2)}{\rho_3^6} - \frac{4\rho_1^2\rho_2^2}{\rho_3^6} + \frac{24a_3^2\rho_1^2\rho_2^2}{\rho_3^8}\right]$$

$$\frac{\partial^2 N}{\partial u\partial v} = \frac{1}{4}\left[\frac{4v(a_1\rho_2^2 + a_2\rho_1^2)}{\rho_3^4} - \frac{8a_3v\rho_1^2\rho_2^2}{\rho_3^6} - \frac{8v(a_1\rho_2^2 + a_2\rho_1^2)}{\rho_3^6} + \frac{24a_3v\rho_1^2\rho_2^2}{\rho_3^8}\right]$$

$$\frac{\partial^2 N}{\partial v^2} = \frac{1}{4}\left[\frac{2(\rho_1^2 + \rho_2^2) + 4v^2(\rho_1^2 + \rho_2^2)}{\rho_3^4} - \frac{8v^2(\rho_1^2 + \rho_2^2)}{\rho_3^6} - \frac{4\rho_1^2\rho_2^2}{\rho_3^6} + \frac{24v^2\rho_1^2\rho_2^2}{\rho_3^8}\right]$$

Step 2: Second-order derivatives of $\Omega_1(u, v) = \frac{(1-\mu)\rho_1^4 + \mu\rho_2^4}{8\rho_3^2}$

$$\begin{aligned}\frac{\partial^2\Omega_1}{\partial u^2} = \frac{1}{512\rho_3^2}\Bigg[&256\mu(\rho_2^2 + 2a_2^2) - 256(1-\mu)(\rho_1^2 + 2a_1^2) \\ &- \frac{64(\mu\rho_2^2 a_2 - (1-\mu)\rho_1^2 a_1)(4a_3)}{\rho_3^2} - 2\frac{\mu\rho_2^4 - (1-\mu)\rho_1^4}{\rho_3^2} \\ &+ \frac{(\mu\rho_2^4 - (1-\mu)\rho_1^4)(4a_3)^2}{\rho_3^4}\Bigg]\end{aligned}$$

$$\begin{aligned}\frac{\partial^2\Omega_1}{\partial u\partial v} = \frac{v}{\rho_3^2}\Bigg[&\mu a_2 - (1-\mu)a_1 - \frac{\mu\rho_2^2 - (1-\mu)\rho_1^2}{\rho_3^2}a_3 \\ &- \frac{\mu\rho_2^2 a_2 - (1-\mu)\rho_1^2 a_1}{\rho_3^2} + \frac{\mu\rho_2^4 - (1-\mu)\rho_1^4}{\rho_3^4}a_3\Bigg]\end{aligned}$$

$$\begin{aligned}\frac{\partial^2\Omega_1}{\partial v^2} = \frac{1}{\rho_3^2}\Bigg[&v^2(\mu - (1-\mu)) + \frac{1}{2}\left(\mu\rho_2^2 + (1-\mu)\rho_1^2\right) \\ &- \frac{v^2(\mu\rho_2^2 - (1-\mu)\rho_1^2)}{\rho_3^2} + \frac{1}{4}\frac{(\mu\rho_2^4 - (1-\mu)\rho_1^4)(4v^2 - \rho_3^2)}{\rho_3^4}\Bigg]\end{aligned}$$

Step 3: Second-order derivatives of $\Omega_2(u,v) = 2\rho_3\left(\frac{\mu}{\rho_2^2} + \frac{1-\mu}{\rho_1^2}\right)$

$$\begin{aligned}\frac{\partial^2\Omega_2}{\partial u^2} &= \frac{4\sqrt{\rho_3^2}\left[-\mu\rho_1^6\rho_2^2 + 4\mu\rho_1^6a_2^2 - (1-\mu)\rho_1^2\rho_2^6 - 4(1-\mu)a_1^2\rho_2^6\right]}{\rho_1^6\rho_2^6} \\ &+ \frac{2\left[\mu\rho_1^2 + (1-\mu)\rho_2^2\right]}{\rho_1^2\rho_2^2\sqrt{\rho_3^2}} - \frac{8\left[\mu\rho_1^4a_2 + (1-\mu)a_1\rho_2^4\right]a_3}{\rho_1^4\rho_2^4\sqrt{\rho_3^2}} \\ &- \frac{2a_3^2\left[\mu\rho_1^2 - (1-\mu)\rho_2^2\right]}{\rho_1^2\rho_2^2\rho_3^3}\end{aligned}$$

$$\begin{aligned}\frac{\partial^2\Omega_2}{\partial u\partial v} &= \frac{8v\sqrt{\rho_3^2}\left[-\mu\rho_1^4a_2 + (1-\mu)a_1\rho_2^4\right]}{\rho_1^4\rho_2^4} - \frac{4v\left[\mu\rho_1^2 + (1-\mu)\rho_2^2\right]a_3}{\rho_1^2\rho_2^2\sqrt{\rho_3^2}} \\ &- \frac{2v\left[\mu\rho_1^4 - (1-\mu)\rho_2^4\right]}{\rho_1^4\rho_2^4\sqrt{\rho_3^2}} + \frac{6va_3^2\left[\mu\rho_1^2 - (1-\mu)\rho_2^2\right]}{\rho_1^2\rho_2^2\rho_3^4}\end{aligned}$$

$$\begin{aligned}\frac{\partial^2\Omega_2}{\partial v^2} &= \frac{4\sqrt{\rho_3^2}\left[-\mu\rho_1^6 + (1-\mu)\rho_2^6\right]}{\rho_1^6\rho_2^6} + \frac{2\left[\mu\rho_1^2 + (1-\mu)\rho_2^2\right]}{\rho_1^2\rho_2^2\sqrt{\rho_3^2}} \\ &- \frac{8v^2\left[\mu\rho_1^4 + (1-\mu)\rho_2^4\right]}{\rho_1^4\rho_2^4\sqrt{\rho_3^2}} + \frac{2v^2\left[\mu\rho_1^2 - (1-\mu)\rho_2^2\right](6a_3^2 - \rho_3^2)}{\rho_1^2\rho_2^2\rho_3^5}\end{aligned}$$

Step 4: Total second derivatives of $\Omega(u,v)$

$$\begin{aligned}\frac{\partial^2\Omega}{\partial u^2} &= \frac{\partial^2\Omega_1}{\partial u^2} + \frac{\partial^2\Omega_2}{\partial u^2} \\ \frac{\partial^2\Omega}{\partial u\partial v} &= \frac{\partial^2\Omega_1}{\partial u\partial v} + \frac{\partial^2\Omega_2}{\partial u\partial v} \\ \frac{\partial^2\Omega}{\partial v^2} &= \frac{\partial^2\Omega_1}{\partial v^2} + \frac{\partial^2\Omega_2}{\partial v^2}\end{aligned}$$

Step 5: Final expressions for the Hessian of $\Omega^*(u,v)$

$$\boxed{\frac{\partial^2\Omega^*}{\partial u^2} = \frac{\partial^2 N}{\partial u^2}\left(\Omega - \tfrac{1}{2}C\right) + 2\frac{\partial N}{\partial u}\cdot\frac{\partial\Omega}{\partial u} + N\cdot\frac{\partial^2\Omega}{\partial u^2}}$$

$$\boxed{\frac{\partial^2\Omega^*}{\partial u\partial v} = \frac{\partial^2 N}{\partial u\partial v}\left(\Omega - \tfrac{1}{2}C\right) + \frac{\partial N}{\partial u}\cdot\frac{\partial\Omega}{\partial v} + \frac{\partial N}{\partial v}\cdot\frac{\partial\Omega}{\partial u} + N\cdot\frac{\partial^2\Omega}{\partial u\partial v}}$$

$$\boxed{\frac{\partial^2 \Omega^*}{\partial v^2} = \frac{\partial^2 N}{\partial v^2}\left(\Omega - \tfrac{1}{2}C\right) + 2\frac{\partial N}{\partial v} \cdot \frac{\partial \Omega}{\partial v} + N \cdot \frac{\partial^2 \Omega}{\partial v^2}}$$

These expressions form the building blocks for constructing the full Hessian matrix $\nabla^2 \Omega^*(u, v)$ used in Newton-type solvers, differential correction, and trajectory optimization in the regularized CR3BP.

B.4 Numerical Validation of Derivatives

In this section, we validate the analytical expressions derived for the gradient and Hessian of the regularized effective potential $\Omega^*(u, v)$, by comparing them against finite-difference numerical approximations. The goal is to assess the accuracy of the symbolic derivatives and ensure their robustness across the full (u, v) domain of interest.

Validation Methodology.

Let $f(u, v) = \Omega^*(u, v)$. We apply the following central finite-difference formulas with step size $h = 10^{-6}$:

$$\begin{aligned}
\frac{\partial f}{\partial u} &\approx \frac{f(u+h,v) - f(u-h,v)}{2h}, \\
\frac{\partial f}{\partial v} &\approx \frac{f(u,v+h) - f(u,v-h)}{2h}, \\
\frac{\partial^2 f}{\partial u^2} &\approx \frac{\frac{\partial f}{\partial u}(u+h,v) - \frac{\partial f}{\partial u}(u-h,v)}{2h}, \\
\frac{\partial^2 f}{\partial u \partial v} &\approx \frac{\frac{\partial f}{\partial u}(u,v+h) - \frac{\partial f}{\partial u}(u,v-h)}{2h}, \\
\frac{\partial^2 f}{\partial v^2} &\approx \frac{\frac{\partial f}{\partial v}(u,v+h) - \frac{\partial f}{\partial v}(u,v-h)}{2h}.
\end{aligned}$$

Example State for Pointwise Validation.

We begin by comparing the analytical and numerical derivatives at a representative state:

- Birkhoff coordinates: $u = 2.8121$, $v = -0.5$
- Velocities: $\dot{u} = 2.0$, $\dot{v} = -3.0$
- Mass parameter: $\mu = 0.01213$ (Earth–Moon system)

First-order derivatives of Ω^*:

Derivative	Analytical	Numerical	Abs. Error
$\partial\Omega^*/\partial u$	$+2.23334557 \times 10^{-1}$	$+2.23334556 \times 10^{-1}$	3.43×10^{-10}
$\partial\Omega^*/\partial v$	$-9.12546348 \times 10^{-2}$	$-9.12546350 \times 10^{-2}$	1.55×10^{-10}

Second-order derivatives of Ω^*:

Derivative	Analytical	Numerical	Abs. Error
$\partial^2\Omega^*/\partial u^2$	$-8.06772503 \times 10^{-3}$	$-8.06772407 \times 10^{-3}$	9.61×10^{-10}
$\partial^2\Omega^*/\partial u\partial v$	$+7.18869463 \times 10^{-2}$	$+7.18869465 \times 10^{-2}$	1.13×10^{-10}
$\partial^2\Omega^*/\partial v^2$	$+1.62895218 \times 10^{-1}$	$+1.62895218 \times 10^{-1}$	9.04×10^{-11}

These results demonstrate excellent agreement between the analytical and numerical values at the test point, with absolute errors well below 10^{-9}, validating the symbolic expressions to high precision.

Domain-Wide Error Maps.

To ensure robustness beyond a single point, we compute derivative errors over a broad mesh in (u, v) that encompasses all five Lagrange points. At each grid point, the base-10 logarithm of the absolute error between analytical and finite-difference derivatives is calculated. The mesh spans the domain

$[-2.5, 2.5] \times [-2, 2]$ with a resolution of 100×100 points. All computations are performed at a fixed Jacobi constant $C = 3.2$, representative of planar motion in the Earth–Moon CR3BP. The resulting error maps are presented below.

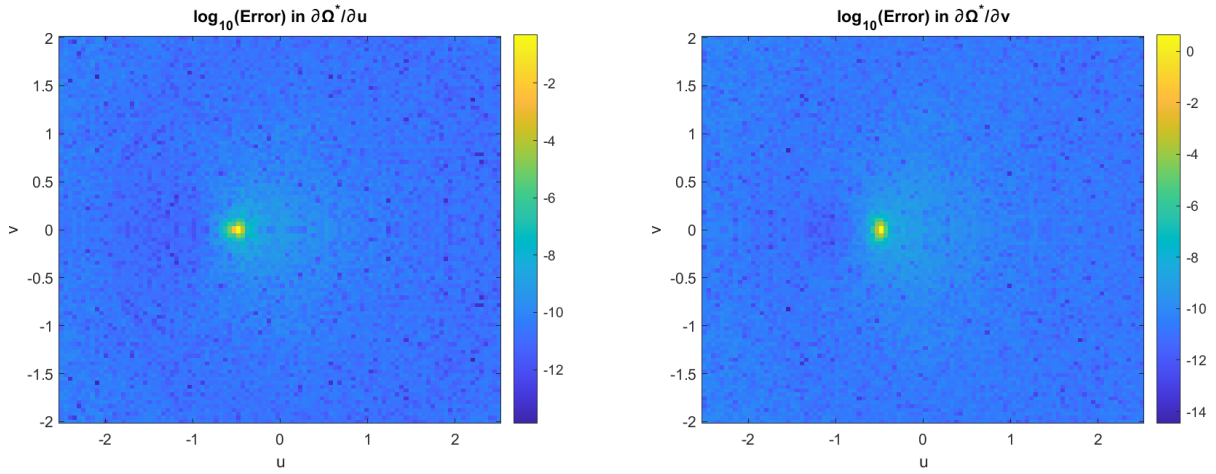

Fig. 19 Log-scale absolute error in $\partial\Omega^*/\partial u$ and $\partial\Omega^*/\partial v$

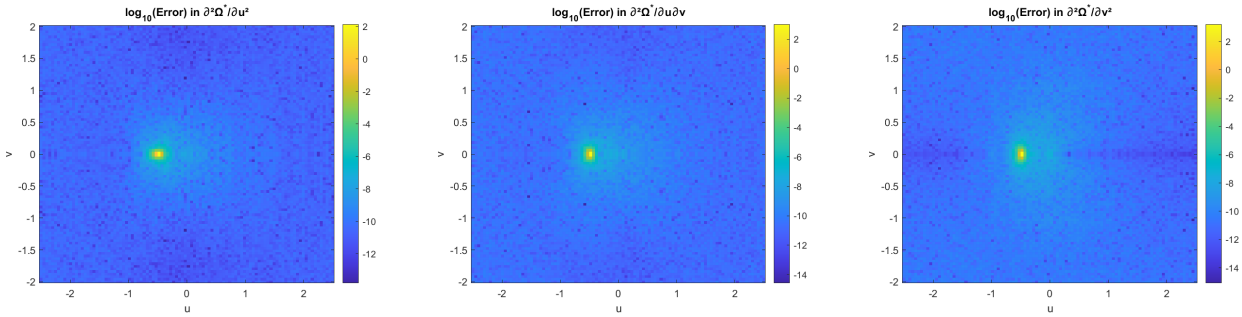

Fig. 20 Log-scale absolute error in $\partial^2\Omega^*/\partial u^2$, $\partial^2\Omega^*/\partial u\partial v$, and $\partial^2\Omega^*/\partial v^2$

Interpretation of Results.

The logarithmic error maps confirm the global accuracy of the analytical derivatives. Errors remain extremely low across the entire domain,typically below 10^{-9}. A localized region of higher error is observed near the singularity at $u \approx -0.5 + \mu$, $v \approx 0$, corresponding to a collision configuration where the transformation becomes ill-conditioned due to near-zero denominators $\rho_3 = \sqrt{(u + \frac{1}{2} - \mu)^2 + v^2}$. This is expected and does not affect the practical reliability of the derivatives in typical mission scenarios.

Overall, the analytical gradient and Hessian of $\Omega^*(u, v)$ are shown to be highly accurate and robust, making them well-suited for use in sensitivity analysis, control design, and optimal trajectory generation in the regularized CR3BP framework.

Appendix C: Jacobian and Time Reparametrization

For convenience, we recall the auxiliary quantities:

$$a_1 = u - \mu, \qquad a_2 = u + 1 - \mu, \qquad a_3 = u + \tfrac{1}{2} - \mu, \qquad \rho_i = \sqrt{a_i^2 + v^2} \ \ (i = 1, 2, 3).$$

C.1 Jacobian of the Birkhoff Transformation

The Jacobian matrix of the mapping $(u, v) \mapsto (x, y)$ is defined as:

$$J(u, v) = \begin{bmatrix} \dfrac{\partial x}{\partial u} & \dfrac{\partial x}{\partial v} \\ \dfrac{\partial y}{\partial u} & \dfrac{\partial y}{\partial v} \end{bmatrix}.$$

The corresponding partial derivatives are:

$$\frac{\partial x}{\partial u} = \tfrac{1}{2} + \tfrac{1}{8}\,\frac{\rho_3 - 2a_3^2}{\rho_3^2}, \qquad \frac{\partial x}{\partial v} = -\tfrac{1}{4}\,\frac{a_3 v}{\rho_3^4},$$

$$\frac{\partial y}{\partial u} = \tfrac{1}{4}\,\frac{a_3 v}{\rho_3^4}, \qquad \frac{\partial y}{\partial v} = \tfrac{1}{2} - \tfrac{1}{8}\,\frac{\rho_3 - 2v^2}{\rho_3^2}.$$

C.2 Time Reparametrization

The conformal factor of the transformation, denoted $N(u, v) = |f'(w)|^2$, defines the time scaling between the physical time t and the regularized time τ:

$$\boxed{\frac{dt}{d\tau} = N(u, v) = \frac{\rho_1^2 \rho_2^2}{4\,\rho_3^4}.}$$

Declaration of Use of Artificial Intelligence

ChatGPT (OpenAI, GPT-5) was used exclusively for English grammar correction and phrasing improvements. No AI tool was used to generate or modify the scientific content, data, or figures. All content was reviewed and approved by the authors.

References

[1] T. Levi-Civita. Sur la résolution qualitative du problème restreint des trois corps. *Acta Mathematica*, 30:305–327, 1906. DOI: 10.1007/BF02418563.

[2] K. F. Sundman. Mémoire sur le problème des trois corps. *Acta Mathematica*, 36:105–179, 1913. DOI: 10.1007/BF02422379.

[3] P. Kustaanheimo and E. Stiefel. Perturbation theory of Kepler motion based on spinor regularization. *Journal für die reine und angewandte Mathematik*, 218:204–219, 1965. DOI: 10.1515/crll.1965.218.204.

[4] E. L. Stiefel and G. Scheifele. *Linear and Regular Celestial Mechanics: Perturbed Two-Body Motion, Numerical Methods, Canonical Theory*. Springer-Verlag, Berlin, 1975.

[5] V. G. Szebehely. *Theory of Orbits: The Restricted Problem of Three Bodies*. Academic Press, New York, 1967.

[6] G. D. Birkhoff. The restricted problem of three bodies. *Rendiconti del Circolo Matematico di Palermo*, 39:265–334, 1915.

[7] G. D. Birkhoff. *Dynamical Systems*. American Mathematical Society, Providence, RI, 1927.

[8] T. N. Thiele. Recherches numériques concernant des solutions périodiques d'un cas spécial du problème des trois corps. *Astronomische Nachrichten*, 138(1), 1895.

[9] G. Lemaître. Regularization of the three-body problem. *Vistas in Astronomy*, 1:207–215, 1955. DOI: 10.1016/0083-6656(55)90028-3.

[10] A. Deprit and R. Broucke. Régularisation du problème restreint plan des trois corps par représentations conformes. *Icarus*, 2:207–218, 1963. DOI: 10.1016/0019-1035(63)90016-2.

[11] R. Broucke. Regularizations of the plane restricted three-body problem. *Icarus*, 4:8–18, 1965. DOI: 10.1016/0019-1035(65)90013-8.

[12] A. Deprit, A. Elipe, and S. Ferrer. Linearization: Laplace vs. Stiefel. *Celestial Mechanics and Dynamical Astronomy*, 58:151–201, 1994. DOI: 10.1007/BF00695790.

[13] D. J. Jezewski. Optimal TV-impulse transfer trajectories using Kustaanheimo/Stiefel variables. *AIAA Journal*, 15:390–394, 1977. DOI: 10.2514/3.60631.

[14] A. A. Quarta and G. Mengali. Linear systems approach to multiple-impulse trajectory analysis via regularization. *Journal of Guidance, Control, and Dynamics*, 33:1679–1683, 2010. DOI: 10.2514/1.50133.

[15] D. J. Jezewski. A comparative study of Newtonian, Kustaanheimo/Stiefel, and Sperling/Burdet optimal trajectories. *Celestial Mechanics*, 12:297–315, 1975. DOI: 10.1007/BF01228565.

[16] J. D. Thorne and C. D. Hall. Minimum-time continuous-thrust orbit transfers using the Kustaanheimo–Stiefel transformation. *Journal of Guidance, Control, and Dynamics*, 20:836–838, 1997. DOI: 10.2514/2.4125.

[17] J. B. Willis and Z. Manchester. Convex optimization of relative orbit maneuvers using the Kustaanheimo–Stiefel transformation. In *IEEE Aerospace Conference*, pages 1–7, 2023. DOI: 10.1109/AERO55745.2023.10115535.

[18] R. C. Engels and J. L. Junkins. The gravity-perturbed Lambert problem: a KS variation of parameters approach. *Celestial Mechanics*, 24:3–21, 1981. DOI: 10.1007/BF01228790.

[19] S. Hernandez and M. R. Akella. Lyapunov-based guidance for orbit transfers and rendezvous in Levi-Civita coordinates. *Journal of Guidance, Control, and Dynamics*, 37:1170–1181, 2014. DOI: 10.2514/1.62305.

[20] S. Hernandez and M. R. Akella. Energy preserving low-thrust guidance for orbit transfers in KS variables. *Celestial Mechanics and Dynamical Astronomy*, 125:107–132, 2016. DOI: 10.1007/s10569-016-9677-0.

[21] R. K. Sharma. Analytical approach using KS elements to short-term orbit predictions including j_2. *Celestial Mechanics and Dynamical Astronomy*, 46:321–333, 1989. DOI: 10.1007/BF00051486.

[22] J. L. Junkins and P. Singla. How nonlinear is it? A tutorial on nonlinearity of orbit and attitude dynamics. *Journal of the Astronautical Sciences*, 52(1–2), 2004.

[23] A. Masat, M. Romano, and C. Colombo. Kustaanheimo–Stiefel variables for planetary protection compliance analysis. *Journal of Guidance, Control, and Dynamics*, 45:1286–1298, 2022. DOI: 10.2514/1.G006255.

[24] K. C. Howell and J. V. Breakwell. Almost rectilinear halo orbits. *Celestial Mechanics*, 32:29–52, 1984. DOI: 10.1007/BF01358402.

[25] M. Rossi and M. Guzzo. A Kustaanheimo–Stiefel regularization of the elliptic restricted three-body problem and the detection of close encounters with fast Lyapunov indicators. *Preprint*, 2024.

[26] K. LeGrand, A. Khilnani, and J. Iannamorelli. Bayesian angles-only cislunar space object tracking. In *AAS/AIAA Space Flight Mechanics Meeting*, Austin, TX, 2023.

[27] R. P. Russell. Primer vector theory applied to global low-thrust trade studies. *Journal of Guidance, Control, and Dynamics*, 30:460–472, 2007. DOI: 10.2514/1.22984.

[28] G. Lantoine. *A Methodology for Robust Optimization of Low-Thrust Trajectories in Multi-Body Environments*. PhD thesis, Georgia Institute of Technology, 2010.

[29] R. E. Pritchett. *Strategies for Low-Thrust Transfer Design Based on Direct Collocation Techniques*. PhD thesis, Purdue University, 2020.

[30] Y. Sidhoum and K. Oguri. Indirect forward–backward shooting for low-thrust trajectory optimization in complex dynamics. In *AAS/AIAA Space Flight Mechanics Meeting*, Austin, TX, 2023.

[31] Y. Sidhoum and K. Oguri. On the performance of different smoothing methods for indirect low-thrust trajectory optimization. *The Journal of the Astronautical Sciences*, 70, 2023. DOI: 10.1007/s40295-023-00417-4.

[32] S. Campagnola, B. B. Buffington, T. Lam, A. E. Petropoulos, and E. Pellegrini. Tour design techniques for the Europa Clipper mission. *Journal of Guidance, Control, and Dynamics*, 42:2615–2626, 2019. DOI: 10.2514/1.G004309.

[33] K. Boudad. *Trajectory Design Between Cislunar Space and Sun–Earth Libration Points in a Four-Body Model*. PhD thesis, Purdue University, 2022.

[34] N. Bosanac. *Leveraging Natural Dynamical Structures to Explore Multi-Body Systems*. PhD thesis, Purdue University, 2016.

[35] K. Oguri. Regularization of the circular restricted three-body problem for trajectory optimization. In *AAS/AIAA Space Flight Mechanics Meeting*, 2024. Paper AAS 24-298.

[36] W. S. Koon, M. W. Lo, Jerrold E. Marsden, and S. D. Ross. *Dynamical Systems, the Three-Body Problem and Space Mission Design*. California Institute of Technology, 2006. See pp. 97–100.

[37] Eduard L. Stiefel and Jörg Waldvogel. Généralisation de la régularisation de Birkhoff pour le mouvement du mobile dans l'espace à trois dimensions. *Comptes Rendus de l'Académie des Sciences de Paris*, 260:805, 1965.

[38] Jörg Waldvogel. Quaternions for regularizing Celestial Mechanics: the right way. *Celestial Mechanics and Dynamical Astronomy*, 102(1–3):149–162, 2008. DOI: 10.1007/s10569-008-9124-y.